

Terahertz spectroscopic polarimetry of generalized anisotropic media composed of Archimedean spiral arrays: Experiments and simulations

Daniel J. Aschaffenburg, Michael R. C. Williams, and Charles A. Schmuttenmaer

Citation: *The Journal of Chemical Physics* **144**, 174705 (2016); doi: 10.1063/1.4947469

View online: <http://dx.doi.org/10.1063/1.4947469>

View Table of Contents: <http://scitation.aip.org/content/aip/journal/jcp/144/17?ver=pdfcov>

Published by the [AIP Publishing](#)

Articles you may be interested in

[Polarimetry in turbid, birefringent, optically active media: A Monte Carlo study of Mueller matrix decomposition in the backscattering geometry](#)

J. Appl. Phys. **105**, 102023 (2009); 10.1063/1.3116129

[Polarization rotation of shape resonance in Archimedean spiral slots](#)

Appl. Phys. Lett. **94**, 091912 (2009); 10.1063/1.3097023

[Manipulating optical rotation in extraordinary transmission by hybrid plasmonic excitations](#)

Appl. Phys. Lett. **93**, 021110 (2008); 10.1063/1.2958214

[Second- and third-harmonic generation in birefringent photonic crystals and microcavities based on anisotropic porous silicon](#)

Appl. Phys. Lett. **87**, 241110 (2005); 10.1063/1.2133910

[A frequency stabilization method for diode lasers utilizing low-field Faraday polarimetry](#)

Rev. Sci. Instrum. **76**, 093108 (2005); 10.1063/1.2038305



NEW Special Topic Sections

NOW ONLINE
Lithium Niobate Properties and Applications:
Reviews of Emerging Trends

AIP | Applied Physics
Reviews

Terahertz spectroscopic polarimetry of generalized anisotropic media composed of Archimedean spiral arrays: Experiments and simulations

Daniel J. Aschaffenburg,^{a)} Michael R. C. Williams,^{b)} and Charles A. Schmuttenmaer^{c)}

Department of Chemistry, Yale University, 225 Prospect St., P.O. Box 208107, New Haven, Connecticut 06520-8107, USA

(Received 22 March 2016; accepted 1 April 2016; published online 3 May 2016)

Terahertz time-domain spectroscopic polarimetry has been used to measure the polarization state of all spectral components in a broadband THz pulse upon transmission through generalized anisotropic media consisting of two-dimensional arrays of lithographically defined Archimedean spirals. The technique allows a full determination of the frequency-dependent, complex-valued transmission matrix and eigenpolarizations of the spiral arrays. Measurements were made on a series of spiral array orientations. The frequency-dependent transmission matrix elements as well as the eigenpolarizations were determined, and the eigenpolarizations were found to be elliptically corotating, as expected from their symmetry. Numerical simulations are in quantitative agreement with measured spectra. *Published by AIP Publishing.* [<http://dx.doi.org/10.1063/1.4947469>]

I. INTRODUCTION

Chirality and optical activity are important molecular properties that have been studied for well over 100 years. Measurements were first carried out in the UV and visible regions of the electromagnetic spectrum, and more recently, vibrational circular dichroism (VCD) has become widely studied in the infrared.^{1,2} There is growing interest in extending these capabilities into the far-infrared, or THz, regime. Measuring a broadband THz VCD spectrum is a challenging task given that $\Delta\epsilon/\epsilon \approx 10^{-4}$ to 10^{-6} in the infrared spectral region (ϵ is the molar extinction coefficient), and the overall magnitude of VCD scales roughly as $1/\lambda^2$.³ While Xu *et al.* have measured CD of a lysosome solution at three specific frequencies (1.53, 1.98, and 2.52 THz) using a free electron laser,⁴ the broadband THz-VCD spectrum of a molecular system has not yet been reported.

Access to this type of spectrum will encourage the development of computational efforts to include the determination of VCD in the study of molecular crystals of chiral molecules and achiral molecules that crystallize in structures belonging to chiral space groups. Presently, software packages that allow the computation of VCD spectra are only applicable to the simulation of isolated molecules. The combination of experimentally measured VCD spectra and rigorous calculations will be a tremendous aid in unambiguous assignment of the often overlapping spectral features in this region. This is due to the fact that VCD peaks may be positive or negative, while absorption peaks may only be positive. Finally, the VCD spectrum of these low frequency collective modes will provide valuable information regarding the relatively weak intermolecular interactions,

insight into which is complementary to the information about the molecular backbone obtained from VCD studies in the mid-infrared.

To make progress toward the measurement of THz VCD spectra of molecular systems, which will be quite weak, we have chosen to study the optical properties of lithographically defined Archimedean spiral arrays, which are metamaterials, in the THz frequency range. In addition to being highly interesting in their own right, metamaterials (artificial structures whose size and array period are both much smaller than the wavelength of impinging light) provide an ideal stepping-stone toward measurements of molecular systems for two reasons: (1) metamaterials may be designed to exhibit large polarization effects (optical activity and circular dichroism) in the THz spectral range, making them an invaluable test platform for developing and improving the spectroscopic techniques needed to measure the small effects expected in molecular systems. (2) Metamaterials based on metallic structures can exhibit plasmonic resonances that give rise to highly localized “superchiral fields,” which have been employed to greatly enhance the sensitivity of circular dichroism measurements of biomolecules at visible and near-infrared wavelengths.⁵ In order to apply a similar technique at THz frequencies, the resonances of potentially useful metamaterials need to be characterized, specifically in terms of their polarization properties. In the present work, these spectroscopic polarimetric measurements and simulations have been carried out and analyzed for arrays of Archimedean spirals.

In general, the optical constants of metamaterials can differ substantially from those of their constituents. A particularly interesting aspect of metamaterial design is the possibility of creating structures that exhibit properties that do not occur naturally, such as negative refractive index.⁶ In addition to negative refractive indices, “chiral” metamaterials can exhibit other unique properties and this has led to research into metal screw-hole arrays,⁷ gammadions,^{8–10} split-ring

^{a)}Present address: Department of Chemistry, University of California, Berkeley, Berkeley, CA 94720, USA.

^{b)}Present address: Center for Integrated Nanotechnologies, Los Alamos National Laboratory, Los Alamos, NM 87545, USA.

^{c)}Email: charles.schmuttenmaer@yale.edu

resonators,^{11,12} bilayer U-shaped resonators,^{13,14} bilayer cross wires,¹⁵ free standing meta-foils,¹⁶ helical metamaterials,^{17–21} and spiral metamaterials.^{22–26}

In order to understand the interaction between THz radiation and anisotropic and/or chiral media, it is important to develop methods that fully characterize the THz signal. It has recently been shown that it is possible to measure the polarization state of every spectral component in a broadband THz pulse using a continuously rotating polarizer.^{27–29} A spinning polarizer has been used in other instances. Grayson *et al.* used a mechanically rotating linear polarizer and wave plate to measure the Hall angle of cuprate superconductors in the far-infrared (20–250 cm^{-1} or 0.6–7.5 THz) using an FTIR instrument.³⁰ They also placed a continuously rotating wave plate before the sample to determine the polarization ellipticity. Subsequent design improvements by those researchers increased the accuracy of this approach.³¹ Similar methods have also been developed and shown to work with both narrowband (2.52 THz) and broadband (0.1–2.5 THz) THz spectroscopy for determining Faraday rotation angles.²⁹ Armitage *et al.* have also demonstrated high precision measurements (accuracy of 0.05° , or 1 mrad, and precision of 0.02°) using essentially the same technique employed in the present work, developed a full mathematical description that characterizes the polarization state of THz light,²⁸ and have demonstrated the technique's utility in studying the Kerr rotation from Bi_2Se_3 thin films.³²

In addition to experimental characterization, it is now common practice to model the interaction of light with metamaterial structures using full 3D electromagnetic simulations. In these simulations, the metamaterial structures are represented using a finite mesh or grid of points. The computational cost of the simulation is proportional to the number of grid points required to accurately represent the structure. This presents a complication when modeling spiral metamaterials because accurate representation of curved structures on a finite grid requires a very fine-grained mesh in rectilinear space. However, continuous improvements in computer hardware and the development of software algorithms for multi-threaded, parallel processing have made it possible to perform calculations that involve upwards of 10^6 grid points in a reasonable amount of time.³³

In this paper, THz time-domain spectroscopic polarimetry (THz-TDP) is used to measure the polarization rotation angle, ellipticity angle, and optical density (OD) upon transmission through Archimedean spiral arrays, as described in Section II. A series of spirals that were investigated in which the spiral orientation was changed is described in Section III. Varying this parameter gives insight into the symmetry-dependent transmission properties of Archimedean spirals, as well as providing information for designing structures with desired frequency-dependent characteristics. This is valuable because minor changes in the design parameters result in vastly different polarization states for the transmitted light. Computer simulations using Computer Simulation Technology (CST) Microwave Studio are in quantitative agreement with the measured spectra, allowing a deeper understanding of these responses. In Section IV, the complex transmission matrix and associated eigenpolarizations for a spiral array are determined,

and Section V provides concluding remarks, including a discussion of what will be necessary to use the techniques and results described herein to ultimately measure the broadband THz VCD spectra of chiral molecular systems.

II. EXPERIMENTAL

One advantage of the THz-TDP method is that it can be implemented quite easily using an existing THz time-domain spectroscopy (THz-TDS) apparatus without requiring any new THz emitters or detectors. This makes it easy to change between THz-TDP and other measurements using the same apparatus with virtually no realignment. In the present experiments, the THz-TDP system is based on a standard unamplified THz-TDS setup.^{34,35} A Ti:Sapphire laser (KMLabs Griffin) producing 50 fs pulses at a center wavelength of 800 nm is used to generate and detect the THz pulses. A beam splitter directs 90% of the output from the laser to an interdigitated photoconductive antenna emitter (Batop iPCA 21-05-1000-800-h), while the remaining 10% of the beam is used for THz detection with an identical photoconductive antenna. The emitter is modulated with a 30 kHz square wave with an amplitude of ± 10 V. The emitter generates linearly polarized light, and the detector is sensitive to linearly polarized light, and they are oriented to generate and detect vertically polarized THz radiation.

A schematic diagram of the THz portion of experimental apparatus, which is purged with nitrogen gas to reduce absorption by atmospheric water vapor, is shown in Figure 1. A free-standing wire-grid polarizer (13 μm wire diameter, 25 μm spacing) is used to “clean up” the nominally vertically polarized THz light from the emitter. The second polarizer (manufactured by Tydex and consisting of 1200 grooves/mm of aluminum on a high density polyethylene substrate) is mounted on a modified optical chopper wheel and spun

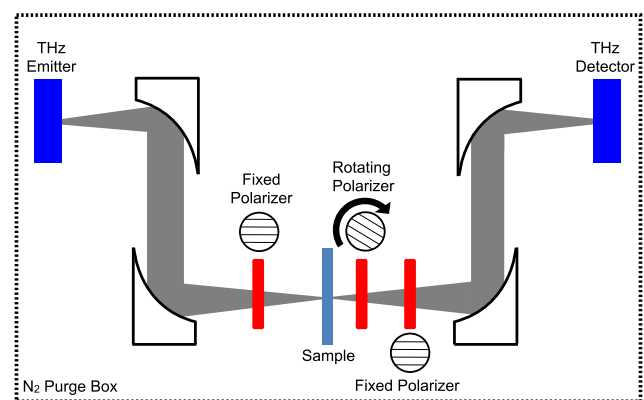


FIG. 1. Schematic diagram of THz-TDP apparatus. Four off-axis paraboloidal mirrors guide and focus the THz pulse from the emitter, through the sample (light blue), and then to the detector. Polarizer positions are indicated in red with an adjacent circle that illustrates their orientation if viewed along the beam path. The first fixed polarizer is used to clean up the vertically polarized THz pulse. The rotating polarizer and the second fixed polarizers are placed after the sample and are used to measure the full polarization state of the transmitted THz pulse. The THz setup is purged with N_2 to avoid absorption of THz by water vapor. Reprinted with permission from Appl. Phys. Lett. **100**, 241114 (2012). Copyright 2012 AIP Publishing LLC.

continuously at 15 Hz (900 rpm). An additional free-standing wire-grid polarizer (13 μm wire diameter, 25 μm spacing), which, like the first polarizer, is fixed at an angle to pass vertically polarized THz light, is placed after the rotating polarizer. A double modulation scheme is used wherein one lock-in amplifier (Stanford Research System SR830) is referenced to the 30 kHz square wave bias voltage used to modulate the THz emission from the photoconductive antenna, and its output is sent into a second lock-in amplifier (same model), which uses a reference frequency of 30 Hz, twice the polarizer rotation frequency.²⁷

The Archimedean spiral arrays were prepared on a 1 mm thick high-resistivity float-zone silicon wafer using electron-beam lithography (Vistec EBPG5000plus). The spirals themselves are made of aluminum and are 250 nm thick. An Archimedean spiral is defined by the function $r(\theta) = a + b\theta$, where r is the distance from the origin and θ is an angle (note that θ is not limited to the range $0-2\pi$). The parameter a specifies the radial offset between the starting point of the spiral and the coordinate system origin. The spacing between turns is given by $b/2\pi$. The spiral's total length can be calculated using

$$L = \int_0^{n2\pi} \sqrt{r^2 + \left(\frac{dr}{d\theta}\right)^2} d\theta, \quad (1)$$

where n is the number of turns. It is somewhat easier to calculate the length if the spiral is defined as $r(\theta) = b\theta$, where θ ranges from θ_1 to θ_2 , with $\theta_1 = 2\pi \cdot a/b$ and $\theta_2 = \theta_1 + n2\pi$

$$\begin{aligned} L &= \int_{\theta_1}^{\theta_2} \sqrt{r^2 + \left(\frac{dr}{d\theta}\right)^2} d\theta = \int_{\theta_1}^{\theta_2} \sqrt{b^2\theta^2 + b^2} d\theta \\ &= b \int_{\theta_1}^{\theta_2} \sqrt{\theta^2 + 1} d\theta \\ L &= b \left[\frac{\theta\sqrt{\theta^2 + 1}}{2} \right]_{\theta_1}^{\theta_2} + \frac{1}{2} \ln \left(\theta + \sqrt{\theta^2 + 1} \right) \Big|_{\theta_1}^{\theta_2}. \end{aligned} \quad (2)$$

The “reference spirals” have an 80 μm array period, 4 μm turn spacing, 4 turns, and a spiral orientation angle of 90° (Figure 2). All spirals are left-handed (counterclockwise rotation when beginning at the center of the spiral and moving

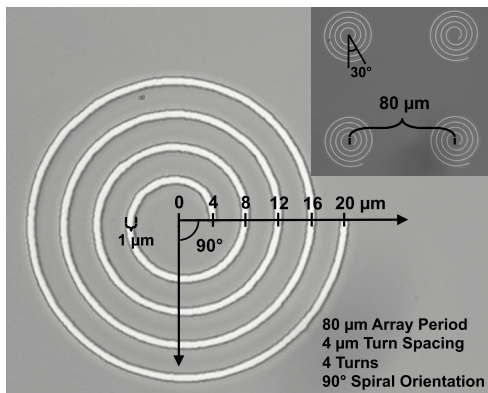


FIG. 2. Optical image of an Archimedean spiral. The reference spirals have a 4 μm turn spacing, 4 turns, 90° spiral orientation, and an 80 μm array period. All spirals have a width of 1 μm . The inset shows the square lattice arrangement with an 80 μm array period and 30° spiral orientation.

outward) and have a 1 μm line width. The spirals are arranged in a square lattice (Figure 2 inset) with a total array size of 5 mm \times 5 mm. During these measurements, the wafer was oriented with the lithographic structures facing the incoming THz beam (see Figure S1 for optical images of all spiral arrays³³).

Finite difference time-domain (FDTD) simulations were performed using the time-domain solver in CST Microwave Studio. The arrays were modeled using a single spiral with periodic boundary conditions in the x and y directions and perfectly matched layer boundaries in the z (propagation) direction, thereby modeling an entire array of spirals, not just one individual spiral. The spiral was modeled as lossy aluminum with a conductivity of 1.5×10^7 S/m, and the substrate was modeled as loss-free silicon with a relative permittivity of 11.69. Using the hexahedral mesh type, the local mesh setting for the spiral had a maximum step of 0.5 μm in the x , y , and z directions. Under these simulation settings, the reference spiral array was modeled using 3.7×10^6 mesh cells. The excitation source was an x -polarized plane wave traveling in the negative z direction with bandwidth from 0 to 3.5 THz. An electric field probe was placed 110 μm after the 1 mm thick Si wafer to collect the x -, y -, and z -polarized electric fields for post-processing. See Table S1 and Figure S2 for information on the time required to run the simulations.³³

III. RESULTS AND DISCUSSION

As described in our recent paper,²⁷ THz-TDP allows both the x and y electric field amplitudes, A_x and A_y , to be determined simultaneously in the time domain. Fourier transformation then yields the amplitude and phase of every spectral component in the frequency domain for both the x and y polarizations: $A_x(\omega)$, $A_y(\omega)$, $\delta_x(\omega)$, and $\delta_y(\omega)$. Using the following equations, these four quantities determine the polarization rotation angle $\phi(\omega)$ and signed ellipticity $\varepsilon_{\pm}(\omega)$ of the transmitted THz pulse, where positive ellipticity is right-handed and negative ellipticity is left-handed (see inset of Figure 3):^{33,36,37}

$$\tan 2\phi(\omega) = \frac{2A_x(\omega)A_y(\omega)}{A_x^2(\omega) - A_y^2(\omega)} \cos(\delta_y(\omega) - \delta_x(\omega)) \quad (3)$$

$$\sin 2\varepsilon_{\pm}(\omega) = \frac{2A_x(\omega)A_y(\omega)}{A_x^2(\omega) + A_y^2(\omega)} \sin(\delta_y(\omega) - \delta_x(\omega)). \quad (4)$$

Figure 3 displays the polarization rotation angle (red), ellipticity angle (black), and optical density (OD, defined as $I = I_0 10^{-\text{OD}}$, blue) of the transmitted THz pulse through the reference spiral arrays over the range of 0.25–2.0 THz (experimentally determined quantities are shown with thick lines and simulation results with thin lines). The polarization rotation angle has two positive features at 0.81 THz and 1.00 THz and one negative feature at 1.13 THz, while the ellipticity angle has two main resonances at 0.83 and 1.07 THz. The OD has a very broad feature at 1.37 THz with shoulders at 1.03 and 1.13 THz and smaller features at 0.59 and 0.81 THz. The broad feature in the OD at 1.37 THz does not have an obvious counterpart in the polarization rotation or ellipticity angle plots.

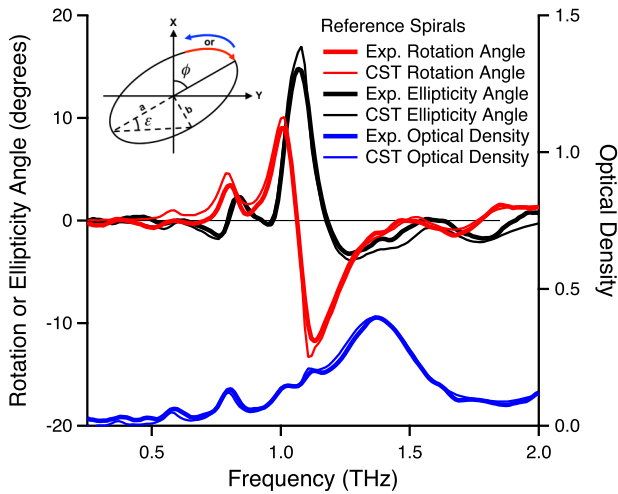


FIG. 3. Rotation angle (red), ellipticity angle (black), and optical density (blue) of the reference spirals. The experimental results are shown with thick lines and the CST results in thin lines of the same color. The inset ellipse indicates the definitions of the polarization rotation angle and ellipticity angle, as well as the handedness.

It is seen that there is quantitative agreement between the experimental and simulation results for the polarization rotation angle, ellipticity angle, and OD. A certain amount of care is needed to achieve this level of agreement when selecting simulation parameters such as the material properties of the silicon substrate and aluminum spiral. For example, the permittivity of the simulated substrate can have a significant influence on the results. The default value for the permittivity of loss-free silicon in the CST material library is 11.9, whereas the literature value for the refractive index of high resistivity silicon in the THz regime is 3.4175,³⁸ corresponding to a permittivity of ~ 11.68 ($\epsilon = n^2$). The resonances shift to lower frequency as the permittivity is increased from 11 to 13 as seen in Figure S3(a),³³ which has also been observed previously.³⁹ Using THz-TDS, we experimentally determined the permittivity for the actual silicon wafer used in the present work to be 11.69, and that is the value used for accurate simulations of our samples.

The default material for metal structures in CST is a perfect electric conductor (PEC). While using PEC for metals reduces the computational cost due to easier meshing and simplifies the simulation because there are no losses, this approximation significantly decreases the accuracy, as seen in Figure S3(b).³³ Modeling the spiral as PEC overestimates the magnitude of polarization rotation and also predicts small oscillations in the 0.5–1.0 THz region that are not observed experimentally. Using aluminum rather than PEC for the spiral material dramatically improves the simulation quality, and therefore, aluminum was chosen over PEC for the spiral material.

While modeling the spiral as aluminum is better than as PEC, the agreement is not perfect. Therefore, the actual value chosen for its conductivity must be considered. The default value in the CST material library for aluminum is its bulk value of 3.56×10^7 S/m. However, Laman and Grischkowsky found that the conductivity of thin Al films with thicknesses of 36, 88, and 152 nm had reduced conductivities of 45%, 42%, and 58% of the bulk value, respectively.⁴⁰ Figure S3(c) shows the effect of systematically decreasing the conductivity of aluminum from 5.0 to 0.5×10^7 S/m.³³ As the conductivity is decreased, the magnitude of the polarization rotation decreases and the resonances shift toward lower frequencies. The optimal value for the conductivity of aluminum was found to be 1.5×10^{-7} S/m, or 42% of the bulk value.

Having determined the optimal values of Si permittivity and Al conductivity, the frequency-dependent polarization rotation angle, ellipticity angle, and OD were simulated for the samples with variations in spiral orientation.

A. Resonance frequencies

It is seen that there are many resonances in the plots of the polarization rotation angle and ellipticity angle as a function of frequency (Figures 3 and 4). Isik and Esselle have determined an equivalent circuit model and analytical formulas for the inductance and capacitance of monofilar and bifilar Archimedean spirals.⁴¹ The resonance frequency of an LC circuit is given by $f_r = (2\pi\sqrt{LC})^{-1}$ and is calculated to

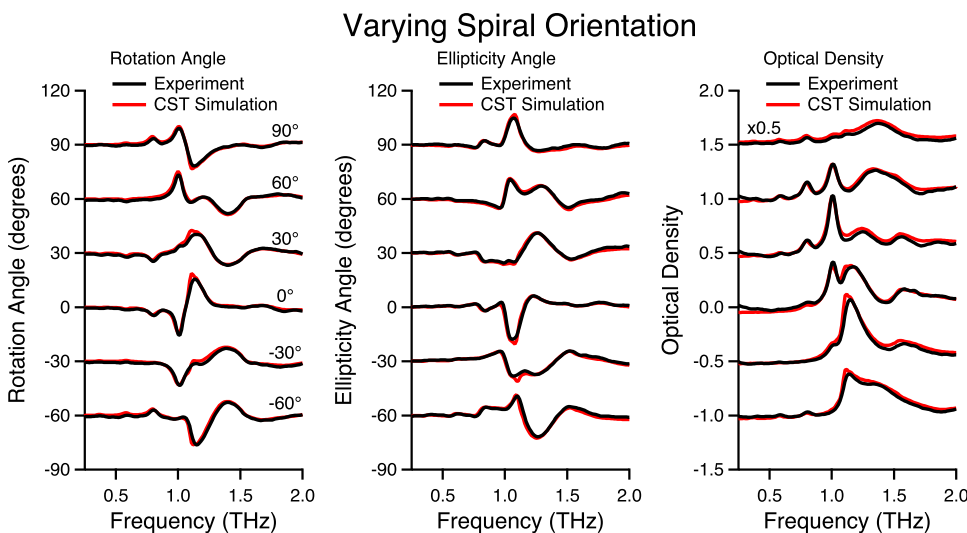


FIG. 4. Rotation angle, ellipticity angle, and optical density for various spiral orientation angles. The spiral orientation angle ranges from 90° to -60° with experimental results in black and CST simulations in red.

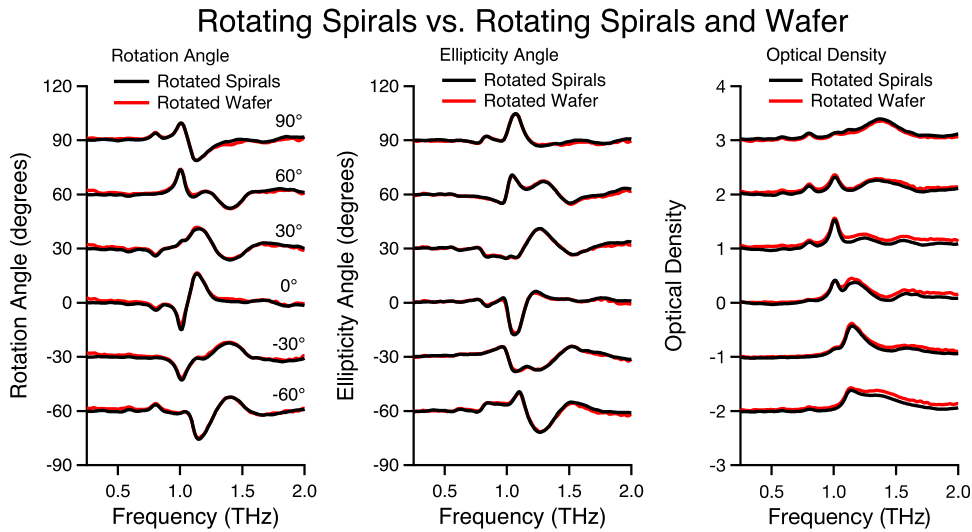


FIG. 5. Rotation angle, ellipticity angle, and optical density comparison of various spiral orientations (black) and lattice arrangements (red).

be 0.136 THz for the “reference spirals” described here. This is lower than the low-frequency cutoff of our spectrometer, but of course is accessible via the CST simulations. This feature appears at 0.163 THz in the CST simulations and differs from 0.136 THz due to approximations in the *LC* circuit model. The approach by Isik and Esselle treats the spiral as a lumped circuit element and does not take into account any structural or geometric resonances. These higher order structural resonances are the origin of the features seen above 0.163 THz (see Figure S4³³).⁴² The surface current maps in the supplementary material show that the resonance at 0.163 THz essentially corresponds to the current in a half-wave dipole antenna when the spiral is unwound.³³ Furthermore, the surface current for the polarization rotation peaks at 0.365, 0.580, 0.793, and 1.006 THz corresponds to full-wave, 3/2-wave, 2-wave, and 5/2-wave, respectively.

Figures S5–S9 display the surface current for these representative frequencies, and animations of the oscillating surface current are available in the supplementary material as well.³³ While some information can be gleaned from the figures and perhaps more from the animations, the progression is far clearer, particularly for the high-order modes, when the surface current is projected onto the spiral and plotted as a function of distance from the beginning of the spiral as shown in Figure S10.³³

B. Spiral orientation

Rotating the spiral orientation yields results quite different from that observed in the other series (see inset in Figure 2 for an example of 30° spiral orientation). As seen in Figure 4, the rotation angle profile for 0° spiral orientation appears to be roughly complementary to the reference spirals with a 90° spiral orientation. This is also the case for 60°/–30° and 30°/–60° pairs. Similar comparisons can be made with the ellipticity angle profiles. On the other hand, the OD results do not follow this trend. While these results initially seem peculiar, the explanation is actually straightforward and is discussed in Section IV A.

An additional experiment was performed that compared spirals rotated within a square lattice with rotating the entire

wafer, thereby rotating both the spirals and the lattice. For example, Figure S11³³ compares rotated spirals but in a square lattice whose horizontal axis remains at 0° with the case where both spirals and lattice are rotated. The experimental results (Figure 5) are identical, indicating that there are no inter-spiral interactions. The results are also essentially identical when the same comparison (rotated spirals in a square lattice vs. rotated spirals and lattice) was simulated with an array period of 60 μm where inter-spiral interactions are likely, indicating that the lattice arrangement does not affect the interaction between the spirals and THz beam (Figure S12³³). The same analysis was performed with 8 turn spirals where the spirals are nearly touching each other, and the results are essentially identical (Figure S12³³). Therefore, the proximity of the spirals is more influential than the lattice orientation when the lattice has fourfold symmetry.

IV. SYMMETRY CONSIDERATIONS AND TRANSMISSION MATRIX

It is possible to use group theory to determine the electromagnetic properties of metamaterials based on the symmetry of the elements comprising them.^{43,44} For example, Archimedean spirals have C_s point group symmetry, the elements of which are the identity operation \hat{E} and a reflection plane $\hat{\sigma}_h$, as seen in Table I.

The irreducible representation for current flow in a spiral of this type is A' ,⁴³ and it is seen that x , y , and R_z transform as A' , and therefore, x - and y -polarized electric fields and z -polarized magnetic fields also transform as A' . More importantly, only x - and y -polarized electric fields and z -polarized magnetic fields may excite or interact with the spirals. The C_s symmetry group results in off-diagonal terms

TABLE I. C_s character table.

C_s	\hat{E}	$\hat{\sigma}_h$		
A'	1	1	x, y, R_z	x^2, y^2, z^2, xy
A''	1	-1	z, R_x, R_y	xz, yz

in the permittivity and magnetoelectric tensors, as well as bianisotropy.

The constitutive relations for a bianisotropic medium are⁴⁵

$$\begin{aligned} \mathbf{D} &= \tilde{\varepsilon} \cdot \mathbf{E} + \tilde{\xi} \cdot \mathbf{H} \\ \mathbf{B} &= \tilde{\zeta} \cdot \mathbf{E} + \tilde{\mu} \cdot \mathbf{H} \end{aligned} \quad (5)$$

where $\tilde{\varepsilon}$ and $\tilde{\mu}$ are the frequency-dependent complex-valued permittivity and permeability tensors, and $\tilde{\xi}$ and $\tilde{\zeta}$ are the magnetoelectric tensors. For a monofilar spiral,⁴⁴

$$\tilde{\varepsilon} = \begin{bmatrix} \varepsilon_{xx} & \varepsilon_{xy} & 0 \\ \varepsilon_{yx} & \varepsilon_{yy} & 0 \\ 0 & 0 & 1 \end{bmatrix}, \quad \tilde{\mu} = \begin{bmatrix} 1 & 0 & 0 \\ 0 & 1 & 0 \\ 0 & 0 & \mu_{zz} \end{bmatrix}, \quad (6)$$

and
$$\tilde{\xi} = -\tilde{\zeta}^T = \begin{bmatrix} 0 & 0 & \xi_{xz} \\ 0 & 0 & \xi_{yz} \\ 0 & 0 & 0 \end{bmatrix},$$

where z is the propagation direction.

A. Transmission matrix

Lederer and co-workers used symmetry arguments and Jones calculus to analyze the transmission properties of metamaterials.⁴⁶ The transmission matrix is a Jones matrix connecting the transmitted field, $\begin{pmatrix} E_{x, out} \\ E_{y, out} \end{pmatrix}$, to the incident field, $\begin{pmatrix} E_{x, in} \\ E_{y, in} \end{pmatrix}$, where all quantities are complex

$$\begin{pmatrix} E_{x, out} \\ E_{y, out} \end{pmatrix} = \begin{pmatrix} T_{xx}e^{i\theta_{xx}} & T_{xy}e^{i\theta_{xy}} \\ T_{yx}e^{i\theta_{yx}} & T_{yy}e^{i\theta_{yy}} \end{pmatrix} \begin{pmatrix} E_{x, in} \\ E_{y, in} \end{pmatrix} = \begin{pmatrix} A & B \\ C & D \end{pmatrix} \begin{pmatrix} E_{x, in} \\ E_{y, in} \end{pmatrix}. \quad (7)$$

It has been shown that all periodic metamaterials may be divided into five distinct symmetry classes, which are referred to as simple anisotropic media, simple chiral media, generalized anisotropic media, generalized chiral media, and arbitrary complex media.⁴⁶ A periodic metamaterial of structures with C_s symmetry is a “generalized anisotropic medium,” and therefore, in Equation (7) above, $B = C$.⁴⁶ The fact that a spiral is superimposable with its mirror image (taken in the xy plane) means that they are not chiral. If the spirals were actually chiral, then the transmission from the front or the back would be identical ($C = -B$ in the transmission matrix⁴⁶), as is the case of a 3-dimensional helix. In contrast, backward transmission through the spiral array reverses the sign of the polarization rotation angle and ellipticity angle.

Since in our experiments the initially vertically polarized THz beam is defined to be x -polarized, Equation (7) becomes

$$\begin{pmatrix} E_{x, out} \\ E_{y, out} \end{pmatrix} = \begin{pmatrix} A & B \\ C & D \end{pmatrix} \begin{pmatrix} E_{x, in} \\ 0 \end{pmatrix}, \quad (8)$$

and A and C can be calculated from simple matrix multiplication

$$A = \frac{E_{x, out}}{E_{x, in}}, \quad (9)$$

$$C = \frac{E_{y, out}}{E_{x, in}}. \quad (10)$$

B and D can be determined by rotating the sample by 90° . A rotation operation of 90° is therefore performed on the transmission matrix as well

$$\begin{pmatrix} \cos(\pi/2) & \sin(\pi/2) \\ -\sin(\pi/2) & \cos(\pi/2) \end{pmatrix} \begin{pmatrix} A & B \\ C & D \end{pmatrix} \begin{pmatrix} \cos(\pi/2) & -\sin(\pi/2) \\ \sin(\pi/2) & \cos(\pi/2) \end{pmatrix} \\ = \begin{pmatrix} D & -C \\ -B & A \end{pmatrix}, \quad (11)$$

and B and D are calculated from this rotated transmission matrix

$$D = \frac{E_{x, out}}{E_{x, in}}, \quad (12)$$

$$-B = \frac{E_{y, out}}{E_{x, in}}. \quad (13)$$

All four complex transmission elements can be obtained directly from the measured x and y THz electric field components. The complex elements A and C are determined from the THz transmission through spirals with 0° spiral orientation and the complex elements D and B are determined from the spirals with spiral orientation of 90° . For the reference spirals, the real components of the complex matrix elements (A' , B' , C' , and D') are plotted in Figure 6(a), and the imaginary components of the complex matrix elements (A'' , B'' , C'' , and D'') are plotted in Figure 6(b). It is seen that B' and C' are superimposable, as are B'' and C'' . The insets in Figure 6 show the differences between B' and C' , and B'' and C'' , respectively, and it is seen that their difference is $\leq 10^3$ of their magnitude. These small differences are attributed to the minor effect of the substrate.⁴⁶ If the substrate is included in the determination of the symmetry, the C_s plane is lost and the material is classified as an “arbitrary complex medium,” for which the off-diagonal matrix elements of the transmission matrix are no longer equal to each other.⁴⁶

The frequency-dependent profiles of B' and B'' are quite similar to the polarization rotation angle and ellipticity angle spectra, respectively. B' determines the in-phase component of the y -polarized field relative to the input x -polarized field and is thereby closely related to the amount of polarization rotation. B'' determines the quadrature component of the y -polarized field relative to the input x -polarized field and is thus closely related to the ellipticity. A' is similar to the optical density because it determines the x -component of the transmitted THz electric field relative to the input x -component of the electric field. The analogous partner of the optical density is the change in phase delay and is closely related to the refractive index, n ,⁴⁷

$$\varphi(d, \nu) - \varphi_0(\nu) = \frac{2\pi\nu(n-1)}{c}d, \quad (14)$$

where ν is the linear frequency, c is the speed of light, φ_0 is the reference phase, φ is the phase after the sample, and d is the path length. The phase delay is closely related to

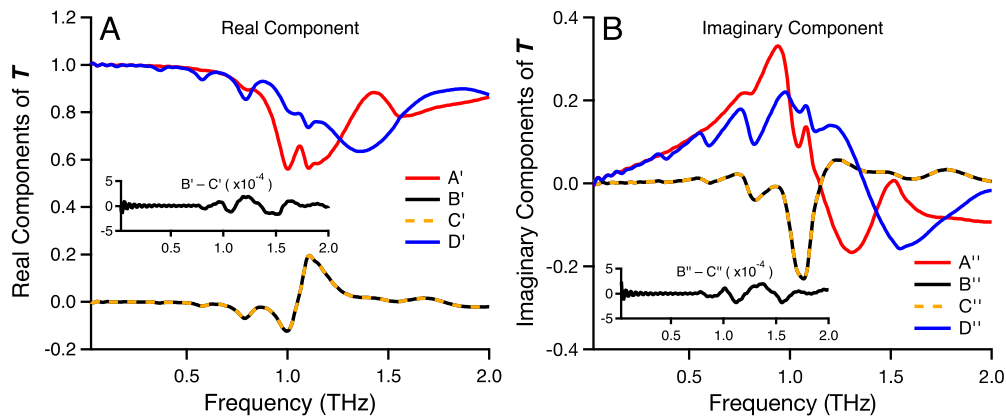


FIG. 6. (a) Real and (b) imaginary components of the transmission matrix elements. Monofilar Archimedean spirals have C_s symmetry and therefore have equal off-diagonal transmission matrix elements. The differences of B' and C' and B'' and C'' due to the presence of the silicon substrate are plotted as insets.

the quadrature component of the transmitted x -polarized field relative to the input field. Thus, A'' and the phase delay have similar frequency-dependent profiles. D is calculated in the same manner as A using the rotated spirals and transmission matrix. Thus, D' and D'' will be similar to the optical density

and phase delay, respectively, for the spirals which are rotated by 90° .

A 90° rotation operation on the transmission matrix has two effects: the A and D matrix elements are interchanged, and B and C are interchanged as well and change sign.

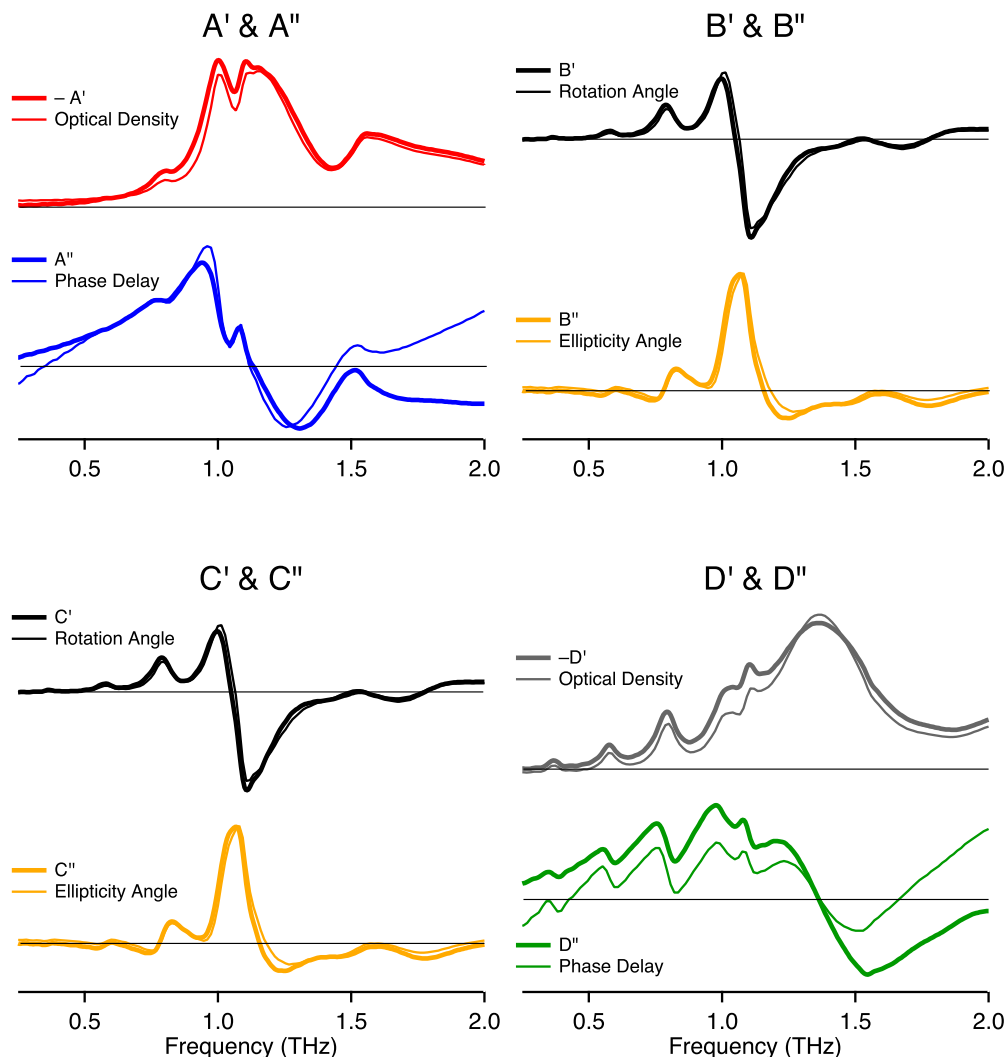


FIG. 7. Comparison of the optical density, change in phase delay, rotation angle, and ellipticity angle (thin lines) for the reference spirals with the appropriate real or imaginary components of the most analogous transmission matrix elements (thick lines). The thin black horizontal lines indicate $y = 0$ to show whether the values are positive or negative. The quantities plotted were arbitrarily scaled to help illustrate the qualitative comparison.

However, since B and C are equal (to within one part in 10^3), the only effect is a change in sign. Therefore, the signs of B' and B'' for spirals with 0° orientation are opposite of that for those with 90° , explaining why the sign of the polarization rotation and ellipticity spectra for spirals with 0° and 90° orientation are nearly opposite, as seen in Figure 4. However, it is observed experimentally that the ODs of spirals with 90° and 0° orientation are not related in a similar manner (Figure 4), which is due to the fact that the values of A' and A'' differ significantly from D' and D'' , respectively.

Figure 7 compares the optical density, phase delay, polarization rotation angle, and ellipticity angle, for spirals rotated by 0° and 90° with the related real or imaginary components of the appropriate transmission matrix elements.

B. Eigenpolarizations

An eigenpolarization is a polarization state of light (polarization angle, ellipticity angle, and handedness) that is transmitted through a material unchanged. For example, the eigenpolarizations for a quarter-wave plate are linearly polarized parallel or perpendicular to the optic axis (the unique axis of a birefringent crystal). Thus, if the optic axis of the crystal is at 0° in some arbitrary coordinate system, the eigenpolarizations are linearly polarized light at 0° and 90° . If the crystal is rotated by 45° , then the eigenpolarizations will be at $\pm 45^\circ$, etc. Linearly polarized light whose polarization plane is not parallel or perpendicular to the optic axis will have its polarization state changed upon transmission through the medium, as will light of any polarization other than linear regardless of the orientation of the crystal relative to the input beam's polarization. Similar arguments may be made with respect to chiral media. In that case, the eigenpolarizations are right- and left-handed circular polarizations, regardless of the sample orientation angle. All linear input polarizations will be changed upon transmission through a chiral material. They may remain linearly polarized, but their polarization angle will change. An elliptical polarization would undergo a change in both ellipticity and polarization angle.

For metamaterials that have elements of C_s symmetry in the xy plane (corresponding to generalized anisotropic media), the two transmission matrix eigenpolarizations are elliptic and corotating, as has been previously observed.⁴⁸ The eigenpolarizations are the eigenvectors of the transmission matrix described in Equation (7).⁴⁶ The eigenvalues of the transmission matrix are

$$\Lambda_{1,2} = \frac{1}{2} \left[(A + D) \pm \sqrt{(A - D)^2 + 4BC} \right] \quad (15)$$

and the eigenvectors (or eigenpolarizations) are

$$\begin{pmatrix} 1 & 1 \\ R_1 e^{i\phi_1} & \frac{1}{R_2} e^{-i\phi_2} \end{pmatrix}, \quad (16)$$

where

$$R_1 e^{i\phi_1} = \frac{X}{2B}, \quad R_2 e^{i\phi_2} = -\frac{X}{2C}, \quad (17)$$

with $X = (D - A) + \sqrt{(A - D)^2 + 4BC}$.⁴⁶ For the reference spirals, the eigenpolarizations are calculated from each eigenvector, and the corresponding frequency-dependent polarization rotation and ellipticity angles are obtained using Equations (3) and (4) and are plotted in Figure 8. The polarization rotation angles of the two eigenpolarizations differ by 90° , while the ellipticity angles are identical, which means that the eigenpolarizations are elliptic corotating (and incidentally, not orthogonal).

The advantage of considering eigenpolarizations rather than transmission matrix elements is that the former are an intrinsic property of the metamaterial. As seen in Figure 4, the polarization rotation angle, ellipticity angle, and optical density of the transmitted THz beam all strongly depend on orientation of the sample. Furthermore, the designation of 0° spiral orientation is arbitrary. On the other hand, the eigenpolarizations are independent of a coordinate system. If the sample were rotated, the only effect would be to shift the curves representing polarization rotation angle of each eigenpolarization up or down by the amount that the

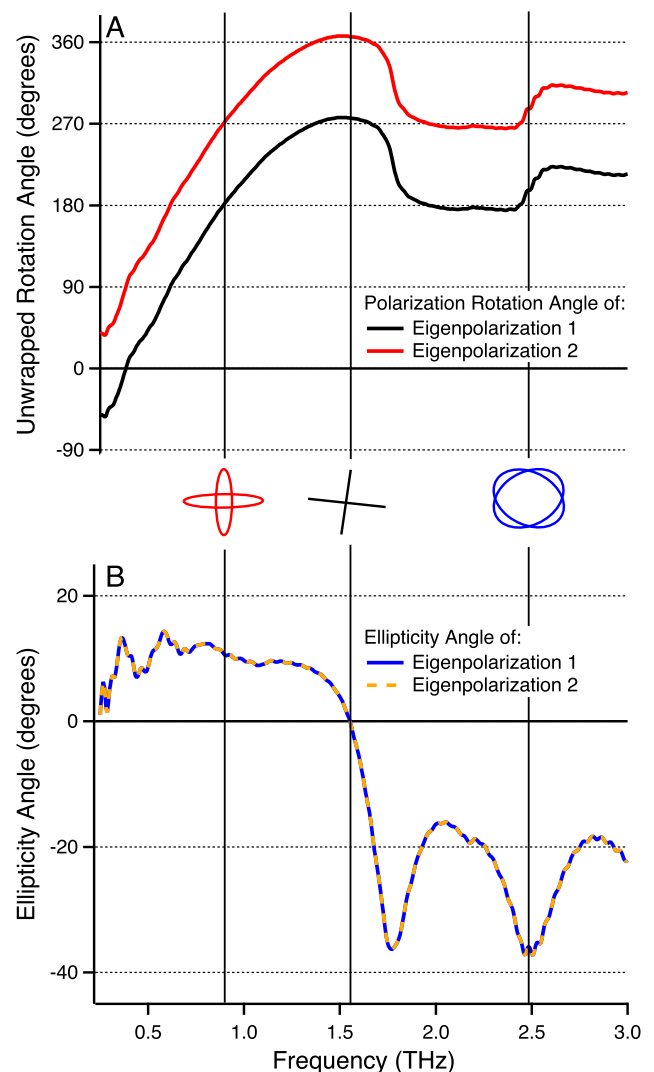


FIG. 8. Polarization rotation (a) and ellipticity angles (b) for both eigenpolarizations determined from the transmission matrix elements. The pictograms in the middle are representations of the polarization state at the given frequency.

sample is rotated. The overall shape of the curves and relation to each other would not change. The ellipticity angle for the eigenpolarizations is in fact completely independent of sample orientation.

V. CONCLUSIONS

We have determined how the polarization rotation angles, ellipticity angles, and optical density of the transmitted broadband THz light depend on spiral orientation. The CST simulations are in excellent agreement with the experimental data for all the configurations studied experimentally.

The frequency-dependent transmission matrix elements as well as the eigenpolarizations were determined using Jones calculus, and the eigenpolarizations were found to be elliptically corotating, as expected from their symmetry. One can now investigate a variety of structures computationally with high confidence prior to cleanroom fabrication. Furthermore, characterization of the influence of varying the geometrical parameters and array spacing of the spirals will aid in the design of metamaterials tailored to exhibit very specific, frequency-dependent polarization effects. The local electromagnetic fields of these resonances may be useful in enhancing the sensitivity of future measurements of the THz VCD spectra of chiral molecules interacting with these structures.

To estimate the sensitivity improvement necessary for the measurement of the THz VCD spectrum of molecular systems, we carried out a density functional theory (DFT) calculation for *S*-ibuprofen, which exhibits strong VCD features in the mid-infrared.⁴⁹ Since it is not possible to calculate the VCD spectrum of molecular solids in existing DFT packages, we modeled the spectrum of the N-shaped dimer of *S*-ibuprofen, using the same basis set and functional as Izumi *et al.*⁴⁹ Our calculation indicates that vibrational modes at approximately 1 THz have a difference in molar extinction coefficient for right-versus left-circularly polarized light of 2×10^{-4} . Converting this to an expected ellipticity angle using the concentration (0.366 mol/l) and path length (0.075 cm) of a typical pressed pellet of solid *S*-ibuprofen yields a value of 0.18°. While the 0.05° accuracy of THz-TDP estimated by Morris *et al.*²⁸ using a wire grid polarizer as a sample suggests that such a relatively large ellipticity angle should be measurable, our preliminary measurements on actual *S*-ibuprofen pellets have been inconclusive. The signal-to-noise ratio (SNR) of the polarization rotation and ellipticity angle measurement is much lower at frequencies where the absorption of the material is high, which is the case for the low-frequency vibrational modes of interest in *S*-ibuprofen. Based on the large number of polarization rotation and ellipticity angle measurements of actual materials in the present work, we estimate a practical accuracy for our THz-TDP apparatus of 0.5°-1.0°. However, mechanical improvements (particularly to the phase stability of the continuously spinning polarizer) may provide sufficient improvement to allow measurement of optical activity and VCD of molecular systems in the THz range. In addition, interactions between molecular systems and the local fields of metamaterial structures like those studied in the present work may provide the necessary enhancement

in sensitivity. Both of these avenues will be explored in future work.

ACKNOWLEDGMENTS

We acknowledge the National Science Foundation (Grant No. CHE-1465085) for partial support of this work. The authors thank Mikhael Guy, Daniel F. Santavicca, and Daniel E. Prober for technical assistance and helpful discussions. This work was supported in part by the facilities and staff of the Yale University Faculty of Arts and Sciences Science Research Software Core.

- ¹R. A. Lombardi and L. A. Nafie, *Chirality* **21**, E277 (2009).
- ²H. Rhee, I. Eom, S. H. Ahn, and M. Cho, *Chem. Soc. Rev.* **41**, 4457 (2012).
- ³P. Atkins and R. Friedman, *Molecular Quantum Mechanics*, 4th ed. (Oxford University Press, Oxford, 2005).
- ⁴J. Xu, J. Galan, G. Ramian, P. Savvidis, A. Scopatz, R. R. Birge, S. J. Allen, and K. Plaxco, in *Chemical and Biological Standoff Detection*, edited by J. O. Jensen and J. M. Theriault (SPIE-Int. Soc. Opt. Eng., USA, 2003), Vol. 5268, p. 19.
- ⁵E. Hendry, T. Carpy, J. Johnston, M. Popland, R. V. Mikhaylovskiy, A. J. Laphorn, S. M. Kelly, L. D. Barron, N. Gadegaard, and M. Kadodwala, *Nat. Nanotechnol.* **5**, 783 (2010).
- ⁶Y. M. Liu and X. Zhang, *Chem. Soc. Rev.* **40**, 2494 (2011).
- ⁷F. Miyamaru and M. Hangyo, *Appl. Phys. Lett.* **89**, 211105 (2006).
- ⁸N. Kanda, K. Konishi, and M. Kuwata-Gonokami, *Opt. Express* **15**, 11117 (2007).
- ⁹N. Kanda, K. Konishi, and M. Kuwata-Gonokami, *Opt. Lett.* **34**, 3000 (2009).
- ¹⁰N. Kanda, K. Konishi, and M. Kuwata-Gonokami, *Opt. Lett.* **37**, 3510 (2012).
- ¹¹R. Singh, E. Plum, C. Menzel, C. Rockstuhl, A. K. Azad, R. A. Cheville, F. Lederer, W. Zhang, and N. I. Zheludev, *Phys. Rev. B* **80**, 153104 (2009).
- ¹²R. Singh, C. Rockstuhl, and W. L. Zhang, *Appl. Phys. Lett.* **97**, 241108 (2010).
- ¹³X. Xiong, W. H. Sun, Y. J. Bao, M. Wang, R. W. Peng, C. Sun, X. Lu, J. Shao, Z. F. Li, and N. B. Ming, *Phys. Rev. B* **81**, 075119 (2010).
- ¹⁴S. Engelbrecht, M. Wunderlich, A. M. Shuvaev, and A. Pimenov, *Appl. Phys. Lett.* **97**, 081116 (2010).
- ¹⁵Y. B. Ding, G. P. Zhang, and Y. Z. Cheng, *Phys. Scr.* **85**, 065405 (2012).
- ¹⁶J. F. Wu, B. H. Ng, S. P. Turaga, M. B. H. Breese, S. A. Maier, M. H. Hong, A. A. Bettiol, and H. O. Moser, *Appl. Phys. Lett.* **103**, 141106 (2013).
- ¹⁷K. J. Chau, M. C. Quong, and A. Y. Elezabi, *Opt. Express* **15**, 3557 (2007).
- ¹⁸A. Y. Elezabi and S. Sederberg, *Opt. Express* **17**, 6600 (2009).
- ¹⁹V. V. Kubarev, V. Y. Prinz, E. V. Naumova, and S. V. Golod, in *34th International Conference on Infrared Millimeter THz Waves* (IEEE, Piscataway, NJ, 2009), Vol. 867.
- ²⁰S. X. Li, Z. Y. Yang, J. Wang, and M. Zhao, *J. Opt. Soc. Am. A* **28**, 19 (2011).
- ²¹F. Hache and G. Gallot, *J. Opt. Soc. Am. B* **29**, 2675 (2012).
- ²²D. K. Wickenden, R. S. Awadallah, P. A. Vichot, B. M. Brawley, E. A. Richards, J. W. M. Spicer, M. J. Fitch, and T. J. Kistenmacher, *IEEE Trans. Antennas Propag.* **55**, 2591 (2007).
- ²³L. D. C. Tzuang, Y. W. Jiang, Y. H. Ye, Y. T. Chang, Y. T. Wu, and S. C. Lee, *Appl. Phys. Lett.* **94**, 091912 (2009).
- ²⁴M. X. He, J. G. Han, Z. Tian, J. Q. Gu, and Q. R. Xing, *Optik* **122**, 1676 (2011).
- ²⁵T. Kan, A. Isozaki, N. Kanda, N. Nemoto, K. Konishi, M. Kuwata-Gonokami, K. Matsumoto, and I. Shimoyama, *Appl. Phys. Lett.* **102**, 221906 (2013).
- ²⁶D. Wang, C. Qiu, and M. Hong, *Appl. Phys. A* **115**, 25 (2014).
- ²⁷D. J. Aschaffenburg, M. R. C. Williams, D. Talbayev, D. F. Santavicca, D. E. Prober, and C. A. Schmuttenmaer, *Appl. Phys. Lett.* **100**, 241114 (2012).
- ²⁸C. M. Morris, R. V. Aguilar, A. V. Stier, and N. P. Armitage, *Opt. Express* **20**, 12303 (2012).
- ²⁹D. K. George, A. V. Stier, C. T. Ellis, B. D. McCombe, J. Cerne, and A. G. Markelz, *J. Opt. Soc. Am. B* **29**, 1406 (2012).
- ³⁰M. Grayson, L. B. Rigal, D. C. Schmadel, H. D. Drew, and P. J. Kung, *Phys. Rev. Lett.* **89**, 037003 (2002).
- ³¹G. S. Jenkins, D. C. Schmadel, and H. D. Drew, *Rev. Sci. Instrum.* **81**, 083903 (2010).

- ³²R. V. Aguilar, A. V. Stier, W. Liu, L. S. Bilbro, D. K. George, N. Bansal, L. Wu, J. Cerne, A. G. Markelz, S. Oh, and N. P. Armitage, *Phys. Rev. Lett.* **108**, 087403 (2012).
- ³³See supplementary material at <http://dx.doi.org/10.1063/1.4947469> for derivation of Eqs. (3) and (4).
- ³⁴M. C. Beard, G. M. Turner, and C. A. Schmuttenmaer, *J. Phys. Chem. B* **106**, 7146 (2002).
- ³⁵M. R. C. Williams, D. J. Aschaffenburg, B. K. Ofori-Okai, and C. A. Schmuttenmaer, *J. Phys. Chem. B* **117**, 10444 (2013).
- ³⁶A. Yariv and P. Yeh, *Optical Waves in Crystals* (Wiley, New York, 1984), p. 62.
- ³⁷E. Castro-Camus and M. B. Johnston, *J. Opt. A: Pure Appl. Opt.* **11**, 105206 (2009).
- ³⁸D. Grischkowsky, S. Keiding, M. Vanexter, and C. Fattinger, *J. Opt. Soc. Am. B* **7**, 2006 (1990).
- ³⁹D. J. Park, S. J. Park, I. Park, and Y. H. Ahn, *Curr. Appl. Phys.* **14**, 570 (2014).
- ⁴⁰N. Laman and D. Grischkowsky, *Appl. Phys. Lett.* **93**, 051105 (2008).
- ⁴¹O. Isik and K. P. Esselle, *IET Microwaves Antennas Propag.* **3**, 929 (2009).
- ⁴²D. F. Santavicca, personal communication (2014).
- ⁴³W. J. Padilla, *Opt. Express* **15**, 1639 (2007).
- ⁴⁴O. Isik and K. P. Esselle, *Metamaterials* **3**, 33 (2009).
- ⁴⁵J. A. Kong, *Electromagnetic Wave Theory* (John Wiley & Sons, New York, 1986).
- ⁴⁶C. Menzel, C. Rockstuhl, and F. Lederer, *Phys. Rev. A* **82**, 053811 (2010).
- ⁴⁷J. T. Kindt and C. A. Schmuttenmaer, *J. Phys. Chem.* **100**, 10373 (1996).
- ⁴⁸E. Plum, V. A. Fedotov, and N. I. Zheludev, *Appl. Phys. Lett.* **94**, 131901 (2009).
- ⁴⁹H. Izumi, A. Ogata, L. A. Nafie, and R. K. Dukor, *J. Org. Chem.* **74**, 1231 (2009).